International Journal of Applied Earth Observation and Geoinformation 144 (2025) 104875

Contents lists available at ScienceDirect

International Journal of Applied Earth Observation and Geoinformation

journal homepage: www.elsevier.com/locate/jag

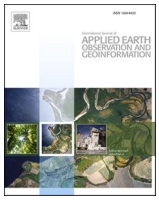

Significant variations in terrestrial water flux in mainland China during 2024 using GRACE-FO: impacts of extreme climate events

Yulong Zhong [a,b], Jingwen Zhou [a,*], Baoming Tian [c], Guodong Xu [d], Yunlong Wu [a]

[a] School of Geography and Information Engineering, China University of Geosciences (Wuhan), Wuhan, China
[b] Institute of Geodesy and Geoinformation, University of Bonn, Bonn, Germany
[c] School of Geospatial Engineering and Science, Sun Yat-Sen University, Zhuhai, China
[d] Department of Land Surveying and Geo-Informatics, The Hong Kong Polytechnic University, Hong Kong, China

ARTICLE INFO

Keywords:
Drought-flood abrupt alternation
GRACE/GRACE-FO
Precipitation change
Terrestrial water flux

ABSTRACT

In 2024, China experiences frequent and severe hydrological extremes, including record-breaking rainfall and widespread droughts, reflecting the intensifying impacts of climate change. The significant changes in terrestrial water storage (TWS) caused by these extreme precipitation events require more detailed analysis to assess short-term hydrological dynamics. Here, we first analyze precipitation anomalies (PA) and percentage of PA (PPA) across mainland China from April to August 2024. The results reveal that PA and PPA in most regions exhibit extreme values in different months, resulting in severe droughts, floods, and abrupt drought-to-flood transitions. To assess the associated water storage changes, we define and apply the terrestrial water flux (TWF), the differenceof GRACE/GRACE-FO-derived TWS anomalies in two adjacent months, as a diagnostic indicator of short-term hydrological variability. Relative to 2002–2024, the grids with TWF percentiles within the 0-10th and 90-100th ranges respectively account for 36.52%, 46.22%, 44.79%, and 46.48% of the total grids from April to August in China. Additionally, 19.89% of grids have the maximum TWF value in 2024. These extremes closely align with variations in precipitation, suggesting that intensified TWF is primarily driven by meteorological factors rather than GRACE-FO data uncertainties. Overall, this study demonstrates the effectiveness of TWF in capturing rapid hydrological changes under climate extremes. The findings provide critical insights into the impacts of climate change on regional hydrological processes and offer a valuable reference for future climate risk management and adaptation strategies at both national and global scales.

1. Introduction

Against the background of climate change, precipitation patterns over global land are experiencing significant transformation, including increased frequency and severity of extreme events (Fischer et al., 2021; Zhang et al., 2021). According to the Intergovernmental Panel on Climate Change (IPCC) Sixth Assessment Report, global temperatures in 2022 are already 1.13 °C higher than pre-industrial levels (IPCC, 2023). This warming trend continues to rise in 2023 and 2024, making 2024 the hottest year on record (World Meteorological Organization, 2024). Such sustained warming has amplified hydroclimatic volatility across many regions (Shu et al., 2024). Swain et al. (2025) showed that global average sub-seasonal (3-month) and interannual (12-month) hydroclimate volatility have respectively increased by 31 %-66 % and 8 %-31 % since the mid-20th century. Wasko et al. (2021) pointed out that climate change has led to an increase in extreme rainfall, especially rare extreme events. These findings highlight the increasing complexity and severity of hydroclimatic extremes under the influence of climate change.

In China, many studies have shown that the likelihood of compound disasters has also risen while extreme heat and rainfall events are increasing significantly (Chen et al., 2020a; China Meteorological Administration, 2024a; Qiao et al., 2022; Wang et al., 2024a). Key drivers of such extreme climate events operate at multiple temporal scales, including annual modes such as El Niño, long-term anthropogenic influences, and changes in atmospheric aerosols (Zou et al., 2025). In 2024, the average temperature in China reaches the highest level since 1961, and precipitation is 10.2 % higher than the historical average, marking the third-highest level on record (following 1998 and 2016) (Zhou, 2024). In April, southern China experienced catastrophic

* Corresponding author.
E-mail address: zhoujingwen@cug.edu.cn (J. Zhou).

https://doi.org/10.1016/j.jag.2025.104875
Received 10 March 2025; Received in revised form 25 August 2025; Accepted 19 September 2025
Available online 25 September 2025

rainstorms and floods (Fig. 1b), with cumulative rainfall at many meteorological stations setting new records (Xinhua News, 2024a). From April to June, severe droughts occurred in North China (Fig. 1c) and the Huanghuai region, followed by drought-to-flood transition due to heavy rains in summer in some provinces (Zhang et al., 2025). In August, drought conditions developed in Sichuan Province, the middle reaches of the Yangtze River, and northwestern Heilongjiang Province (National Climate Centre, 2024a). According to statistics, floods and secondary disasters triggered by continuous extreme precipitation cause a total direct economic loss of 263.04 billion in 2024. Drought disasters resulting from less rainfall and continuous high temperatures inflicted a direct economic loss of 8.36 billion and affected 1.21 million hectares of crops (Ministry of Emergency Management of the People's Republic of China, 2025). In addition to posing serious threats to human survival and economic development, these disasters can also cause great harm to the ecosystem and environment. Qin et al. (2005) revealed that the intensification of extreme climate over the past 50 years has resulted in accelerated glacier retreat, a decline in the regulatory and storage capacity of lakes in the middle and lower reaches of the Yangtze River, 3.56 million km^2 of soil and water loss across China, and agricultural losses in the lower reaches of the Yellow River due to increased industrial and agricultural water use. Yin et al. (2022) pointed out that droughts and precipitation changes will exacerbate soil erosion and land degradation, further deteriorating the ecological environment. The study also projects that approximately 59.8 % of China's population and 57.7 % of its GDP will face moderate to severe drought risks in the future.

These extreme hydrological events can cause substantial changes in

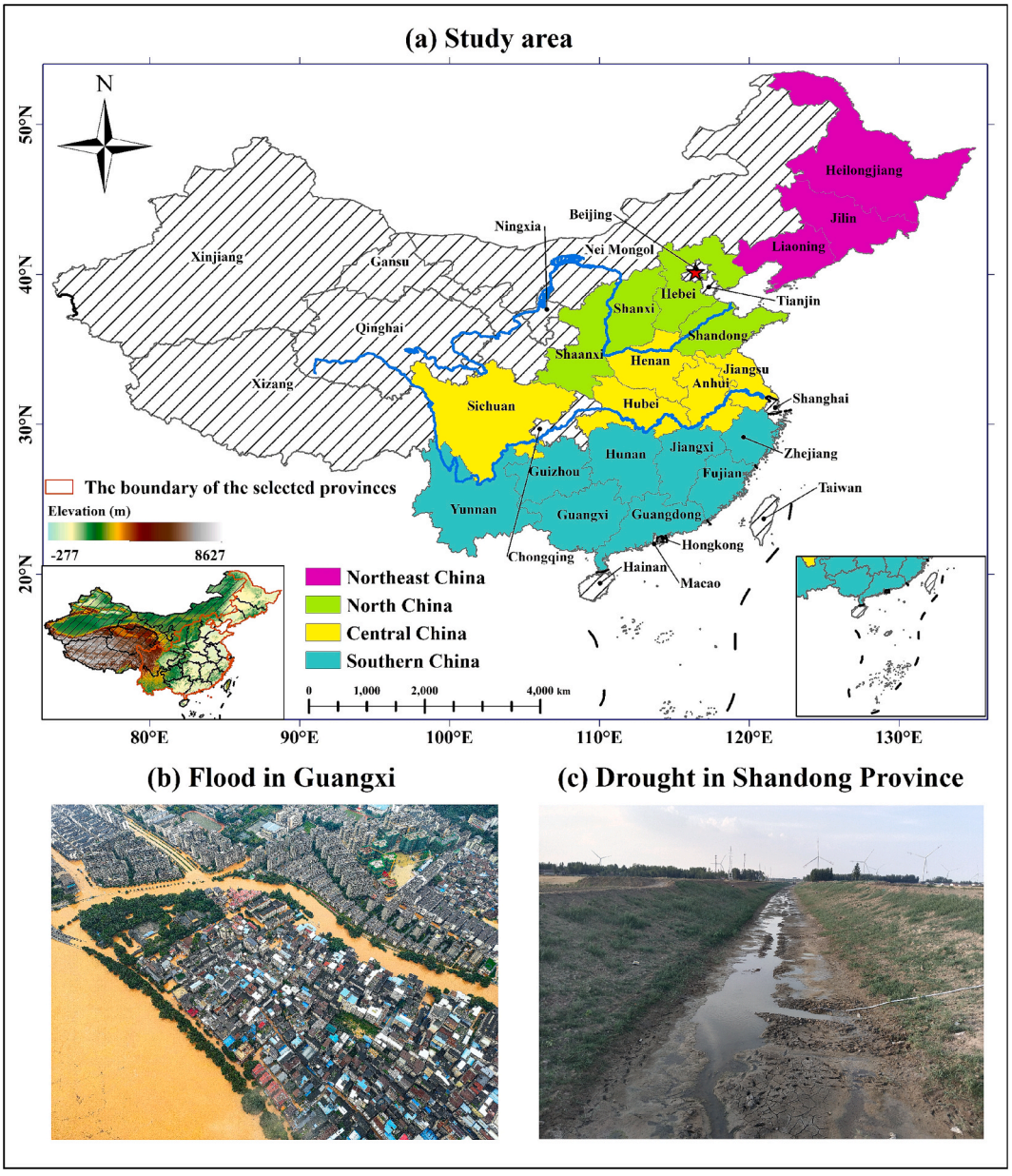

Fig. 1. Map of the study area and on-site photos of two severe drought and flood disasters in China in 2024. (a) Study area. The 20 selected eastern provinces are divided into four distinct parts. Southern China: Guangxi Zhuang Autonomous Region (hereafter referred to as Guangxi), Guangdong, Yunnan, Guizhou, Hunan, Jiangxi, Fujian, Zhejiang Provinces; Central China: Sichuan, Hubei, Anhui, Henan, Jiangsu Provinces; North China: Shaanxi, Shanxi, Hebei, Shandong Provinces; Northeast China: Liaoning, Jilin, Heilongjiang Provinces. The red line is the boundary of selected provinces, excluding Chongqing, Shanghai, Beijing and Tianjin. (b) Flood in Guangxi (© Visual China Group). (c) Drought in Shandong Province (photo by the authors). (For interpretation of the references to colour in this figure legend, the reader is referred to the web version of this article.)

terrestrial water storage (TWS). Therefore, in-depth research and quantification of the changes in TWS in China in 2024 are essential to understanding the potential disaster processes and mechanisms. Since their launch, the Gravity Recovery and Climate Experiment (GRACE) satellite mission and its successor GRACE Follow-On (GRACE-FO) have provided us a new method of quantifying TWS (Chen et al., 2009; Long et al., 2013; Tapley et al., 2019). Unlike traditional ground observation, the GRACE/GRACE-FO satellites can provide dynamic changes in global and regional TWS by measuring changes in the earth's gravity field, which is an effective approach for monitoring large-scale terrestrial water storage anomaly (TWSA) (Pan et al., 2024; Tapley et al., 2004). With their high spatial resolution, GRACE/GRACE-FO data can be widely used in areas where lack ground-based observation stations. Therefore, it has an irreplaceable advantage in global TWS research (Famiglietti and Rodell, 2013; Sun et al., 2020b). Moreover, TWSA associated with extreme climate events can also be precisely captured by GRACE/GRACE-FO, offering valuable insights into the hydrological processes and mechanisms underlying disasters such as extreme precipitation, droughts, and floods (Gerdener et al., 2020; Lai et al., 2025; Xie et al., 2022). Thus, quantifying TWSA using GRACE/GRACE-FO data has become an essential tool in climate change research (Rodell and Li, 2023; Tapley et al., 2019; Wouters et al., 2014). TWS is a comprehensive reflection of surface water, soil moisture, groundwater and other components (Rodell et al., 2018). Its time derivative − TWS change (TWSC) reflects the dynamic water flux. In this study, we calculate terrestrial water flux (TWF), derived from the time derivative of TWSA between two adjacent months (unit: mm/month), which emphasizes the month-to-month fluctuations and abrupt transitions in water storage. Syed et al. (2008) first compared the TWSC simulated by GRACE observations with that by GLDAS, revealing the spatiotemporal variation characteristics of TWS under extreme events. Duan et al. (2024) used TWSC as one of the key indicators to quantify water storage loss during the extreme drought period in the Yangtze River Basin in 2022. Additionally, many relevant studies rely on the water balance method to estimate basin-scale evapotranspiration across various regions (Long et al., 2014; Pan et al., 2017; Ramillien et al., 2006; Rodell et al., 2004) and to analyze water cycle processes (Eicker et al., 2016; Lan et al., 2016). To our best knowledge, few studies directly focus on the dynamic characterization of regional TWS changes by TWF and its response to climate change.

Since TWF captures monthly-scale variations in TWSA, it allows for a refined quantification of hydroclimatic fluctuations and offers a unique perspective on regional water storage dynamics. This analytical advantage is consistent with the findings of Ran et al. (2024), who emphasized the importance of capturing high-frequency water storage variability in understanding extreme hydrological events. As these short-term water storage changes are often triggered by precipitation and temperature anomalies, TWF provides an effective means of assessing the hydrological impacts of climate change. In this context, while 2024 is expected to be a year significantly impacted by meteorological disasters, there is currently a lack of research quantifying the changes in TWSA during this period. This study aims to use TWF to quantify the extremeness of TWSA changes across China in 2024 and explore its driving factors, providing theoretical support for water resources management and disaster prevention and mitigation. To this end, we analyze the precipitation anomalies (PA), TWF percentiles in middle of 2024 relative to the whole 2002–2024 period, and the years and months with the maximum TWF for the period. Furthermore, given that the GRACE-FO data may contain certain inherent errors, this study also discusses the significance and reliability of the 2024 TWF changes within the context of these potential uncertainties.

2. Data and methods

2.1. Study area

China, located in the eastern Asia and along the western Pacific Ocean, is characterized by diverse climate types due to its complex terrain and extensive span of longitude and latitude. It plays a crucial role in global climate systems (Wu, 2023). The eastern regions of China are affected by the East Asian monsoon (Zhang, 2015), resulting in pronounced seasonal and regional variability in precipitation: summer and autumn are typically wet, while spring and winter tend to be dry, with rainfall amounts generally decreasing from south to north. According to the China Flood Risk Map (Zhang et al., 2000), the overall flood loss index in the eastern monsoon region is 2.3 times higher than that in the west, indicating a higher level of disaster impact in eastern China. Moreover, the eastern part of China has a denser network of meteorological observation stations, enabling access to higher-quality and more comprehensive dataset (Han et al., 2022). Therefore, while this study presents national-scale spatial distributions to capture broad spatial variation patterns, the regional-scale analysis focuses on 20 provinces in eastern China, each covering an area of over 100,000 km^2 (Fig. 1). These provinces are selected based on climatic conditions (Domrös and Peng, 2012), data quality (Han et al., 2022; Zhong et al., 2023), human activities (Xie et al., 2019) and other factors, to ensure the robustness of the analysis.

Based on the precipitation distribution observed in this study, we adopt the climate regionalization proposed by Zheng et al. (2013) and divide the eastern part of mainland China into four regions: southern China, central China, North China and Northeast China.

2.2. Data

Table 1 presents the information of data used in this study, including the temporal resolution, spatial resolution, time span, coverage area and data acquisition sources.

2.2.1. GRACE/GRACE-FO data

In this study, we use the CSR RL06.3 Mascon Solutions (CSRM) dataset from the Center for Space Research (CSR) at the University of Texas to estimate changes in TWS. The CSRM has undergone comprehensive corrections, including the replacement of the C20 and C30 coefficients with satellite laser ranging, degree-1 coefficients (geocenter) correction (Swenson et al., 2008), glacial isostatic adjustment (Peltier

Table 1
Information of datasets used in this study.

Dataset	Temporal	Spatial	Time span	Coverage area	Data source
CSRM RL06.3	monthly	0.25°	2002–2024	global	https://www2.csr.utexas.edu/grace/RL06_mascons.html
CHM_PRE	daily	0.5°	1961–2022	China	https://www.tpdc.ac.cn/zh-hans/data/e5c335d9-cbb9-48a6-ba35-d67dd614bb8c
CLDAS-V2.0	daily	0.0625°	2023–2024	Asia	https://data.cma.cn/data/cdcdetail/dataCode/NAFP_CLDAS2.0_NRT.html
ERA5-Land	monthly	0.1°	2000–2024	China	https://cds.climate.copernicus.eu/datasets/reanalysis-era5-land-monthly-means?tab=overview

et al., 2018), and ellipsoid correction (Ditmar, 2018). Therefore, it does not require additional post-processing after released. Compared to spherical harmonic coefficient products, Mascon solutions effectively remove north–south strip noise and signal leakage error (Scanlon et al., 2018; Zhang and Sun, 2022). In addition, mascon gain factors already account for latitudinal striping. GRACE-FO employs improved accelerometers, which mitigate the leak in the cold gas propulsion system, reducing potential errors in the data (Save, 2020). The CSRM dataset provides monthly TWSA from April 2002 to June 2017 (GRACE) and from May 2018 to August 2024 (GRACE-FO), expressed in equivalent water height (unit: cm), with a spatial resolution of 0.25° (actual spatial resolution is approximately 3°). Notably, the CSRM are relative to the 2004–2009 time-mean baseline (Save, 2020).

2.2.2. Precipitation data

The precipitation data employed in this study are sourced from the China Hydro-Meteorology dataset (CHM_PRE), a high-resolution, long-term, gauge-based daily gridded dataset encompassing mainland China from 1961 to 2022 (Han et al., 2022). This dataset is constructed from daily precipitation observations collected at 2,839 stations within and surrounding China. Its reliability for hydrological and climate studies has been validated using 45,992 gauge observations across China from 2015 to 2019 (Han et al., 2022). CHM_PRE offers multiple spatial resolutions: 0.1°, 0.25°, and 0.5°, covering the geographical extent of 18°N − 54°N and 72°E − 136°E. This study utilizes the precipitation data with a spatial resolution of 0.5° from 1961 to 2022, primarily for reconstructing TWSA and calculating PA.

Due to the CHM_PRE dataset's coverage ending in 2022, we supplement the CHM_PRE dataset with data from the China Meteorological Administration Land Data Assimilation System Version 2.0 (CLDAS-V2.0) from 2023 to 2024, which provides hourly and daily gridded precipitation data across the Asian region at a spatial resolution of 0.0625° × 0.0625°. The CLDAS-V2.0 products have been evaluated against observations from over 2,400 national automatic weather stations in China (China Meteorological Administration, 2024b), demonstrating high accuracy within the Chinese region (Sun et al., 2020a; Yang et al., 2017). To ensure consistency with the CHM_PRE dataset, we resample the daily CLDAS-V2.0 data from its original resolution of 0.0625° × 0.0625° to a 0.5° × 0.5° grid by averaging the values of 64 smaller grids (0.0625°) into one larger grid (0.5°), thereby preserving the overall precipitation values.

2.2.3. Soil moisture data

The soil moisture data are obtained from the land component of the fifth generation of European ReAnalysis (ERA5-Land) dataset, released by the European Centre for Medium-Range Weather Forecasts (ECMWF). ERA5-Land offers high-resolution global climate reanalysis data from 1950 to the present (Muñoz-Sabater, 2019). The soil moisture component is segmented into four depth layers: 0–7 cm, 7–28 cm, 28–100 cm, and 100–289 cm. Extensive validation studies have demonstrated the reliability of this dataset in representing soil moisture and other hydrological variables (Muñoz-Sabater et al., 2021). In this study, we utilize monthly gridded soil moisture data from 2000 to 2024, covering four vertical layers with a spatial resolution of 0.1°. Specifically, soil moisture values in each layer are converted into equivalent water thickness and then summed to the dataset for analysis.

2.3. Methods

2.3.1. PA and percentage of PA

PA is defined as the deviation of observed precipitation (P) from the multi-year (1961–2024) mean precipitation ($\overline{P}$) over the same period.

$$PA = P - \overline{P} \tag{1}$$

A negative PA with a large absolute value indicates significantly lower precipitation than the long-term average, suggesting potential drought conditions. Conversely, a positive with a large absolute value signifies higher than average precipitation, implying an increased risk of floods.

To further quantify the degree of precipitation deviation, the percentage of PA (PPA) is calculated. It is an important reference indicator for analyzing abnormal climate changes and assessing drought and flood disasters. The calculation formula is:

$$PPA = \frac{PA}{\overline{P}} \times 100\% \tag{2}$$

This standardized metric provides a clearer representation of PA and facilitates comparisons between different regions.

2.3.2. TWSA reconstruction

Humphrey and Gudmundsson (2019) developed a climate-driven statistical model to reconstruct the detrended and deseasonalized GRACE TWSA using precipitation and temperature data at daily and monthly scales. Further details about the reconstruction method and its implementation can be found in Humphrey and Gudmundsson (2019). Some relevant applications of the method can be referred to studies such as the monitoring the extreme flood event in July 2021 in northern Henan, China (Xiao et al., 2023), the quantification of drought characteristics in exorheic basins in China using a novel daily drought index (Yang et al., 2025), and the estimation of the average daily fraction of precipitation transformed into TWS in global river basins (Zhong et al., 2025). Given the extensive prior work of our research group on this reconstruction method, we focus on applications in this study rather than detailed computational steps, which are thoroughly described in the aforementioned studies.

In this study, we utilize precipitation and temperature data to reconstruct the TWSA over the period 2002 – 2024, with model parameters calibrated under the constraints of CSRM during the GRACE period. This approach aims to reduce observation-specific errors associated with GRACE-FO data and ensure that the differences in reconstructed TWSA fluctuations between the two periods are primarily driven by meteorological factors. Hacker and Kusche (2024) demonstrated that multi-decadal GRACE-like reconstructions can reliably capture both long-term trends and seasonal to sub-seasonal variability, confirming the robustness of our method in distinguishing climate-driven signals from observational uncertainty.

2.3.3. TWF calculation

To emphasize the short-term changes in TWSA over a two-month period under impact of climate change, TWF is defined as the difference of TWSA between two adjacent months. However, the discontinuity in TWSA is caused by missing data from the CSRM, which results from an 11-month gap between the GRACE and GRACE-FO missions and battery failure. Therefore, it is essential to account for the time intervals caused by the missing CSRM data when computing TWF. Specifically, an Interval threshold is applied to judge if the TWF estimates can be used for analyzing in this study.

$$\text{Interval}_{i-1} = \text{time}_i - \text{time}_{i-1} \tag{3}$$

$$\text{TWF} = \text{TWSA}_j - \text{TWSA}_{j-1} \tag{4}$$

where time_i represents the CSRM monthly time point ($i = 2, 3, \ldots, 236$), j denotes the TWSA months as the Interval within the defined threshold.

We assign the "time" variable (unit: days) of CSRM data as the representative time point (time_i) and compute the difference between adjacent time ($\text{Interval}_{i\text{-}1}$) using Eq. (3). According to statistics, the median and mode of Interval are both 30.5 days, accounting for 183 TWF estimates (77.9 % of the total 235). To maximize the inclusion of valid data while maintaining the reliability of the estimates, a 32-day threshold is selected for the Interval. This threshold covers 91.1 % of

total TWF estimates. In addition, the soil moisture flux (SMF) can be also calculated similar to TWF.

2.3.4. Calculation of normalized mean absolute deviations

The mean absolute deviation (MAD) is used to quantify the discreteness or variability of a dataset. In this study, we apply the formula to calculate the difference between the CSRM TWF (TWF_{CSRM}) and the reconstructed TWF (TWF_{REC}). The calculation is expressed as:

$$MAD = \text{mean}(|TWF^{i}_{CSRM} - TWF^{i}_{REC}|) \quad (5)$$

where i is 1 or 2, respectively representing two specific periods of GRACE/GRACE-FO.

To assess the relative significance of MAD compared with the fluctuation of TWF_{CSRM}, two normalization methods are applied. The first method is the MAD ratio (TWF_{MADR}), which is normalized by standard deviation (STD) of TWF_{CSRM}. STD measures the average deviation of data from the mean but is sensitive to extreme values. In contrast, the interquartile range (IQR) defined as the difference between the 75th and 25th percentiles, focusing on the range of variation for the central 50 % of the data, and is less affected by extremes. Accordingly, the scaled MAD (TWF_{SMAD}) is normalized by IQR of TWF_{CSRM}. The formulas are as follows:

$$TWF_{MADR} = \frac{MAD}{STD(TWF^{i}_{CSRM})} \quad (6)$$

$$TWF_{SMAD} = \frac{MAD}{IQR(TWF^{i}_{CSRM})} \quad (7)$$

2.3.5. Precipitation variability

Precipitation variability reflects the fluctuation of precipitation over time, often measured as variance or STD. In a related study, Zhang et al. (2024) employed STD to investigate the century-long changes in precipitation variability on global and regional scales, which was divided into various time scales on regional scale. Additionally, daily precipitation time series were detrended and deseasonalized to remove linear trends and annual cycles. In this study, we directly calculate the STD (STD_{PA}) and IQR (IQR_{PA}) of monthly PA from 2002 to 2024 to quantify the variabilities during the GRACE and GRACE-FO periods.

3. Result

3.1. PA and PPA analysis

In 2024, extreme precipitation events occur across various regions of China, resulting in significant fluctuations in TWS. To evaluate these changes, we first analyze the PA and PPA across China (Fig. 2). The findings reveal distinct regional characteristics, with pronounced deviations in precipitation patterns compared to historical averages, leading to widespread flooding, droughts, and abrupt transitions between these extremes.

In southern China, PA values exhibit substantial positive anomalies in April and June, such as Hunan (102.78 mm and 145.57 mm), Jiangxi (189.79 mm and 154.16 mm), and Zhejiang (131.17 mm and 169.40 mm) Provinces (Table 2), indicating that precipitation significantly exceeds historical norms in these areas. According to official statistics, the cumulative precipitation in South China is 40 % higher than the annual average during the pre-flood season, and the cumulative precipitation exceeds 500 mm in many provinces from June 2 to July 9 (China Meteorological Administration, 2025). Conversely, in May, July and

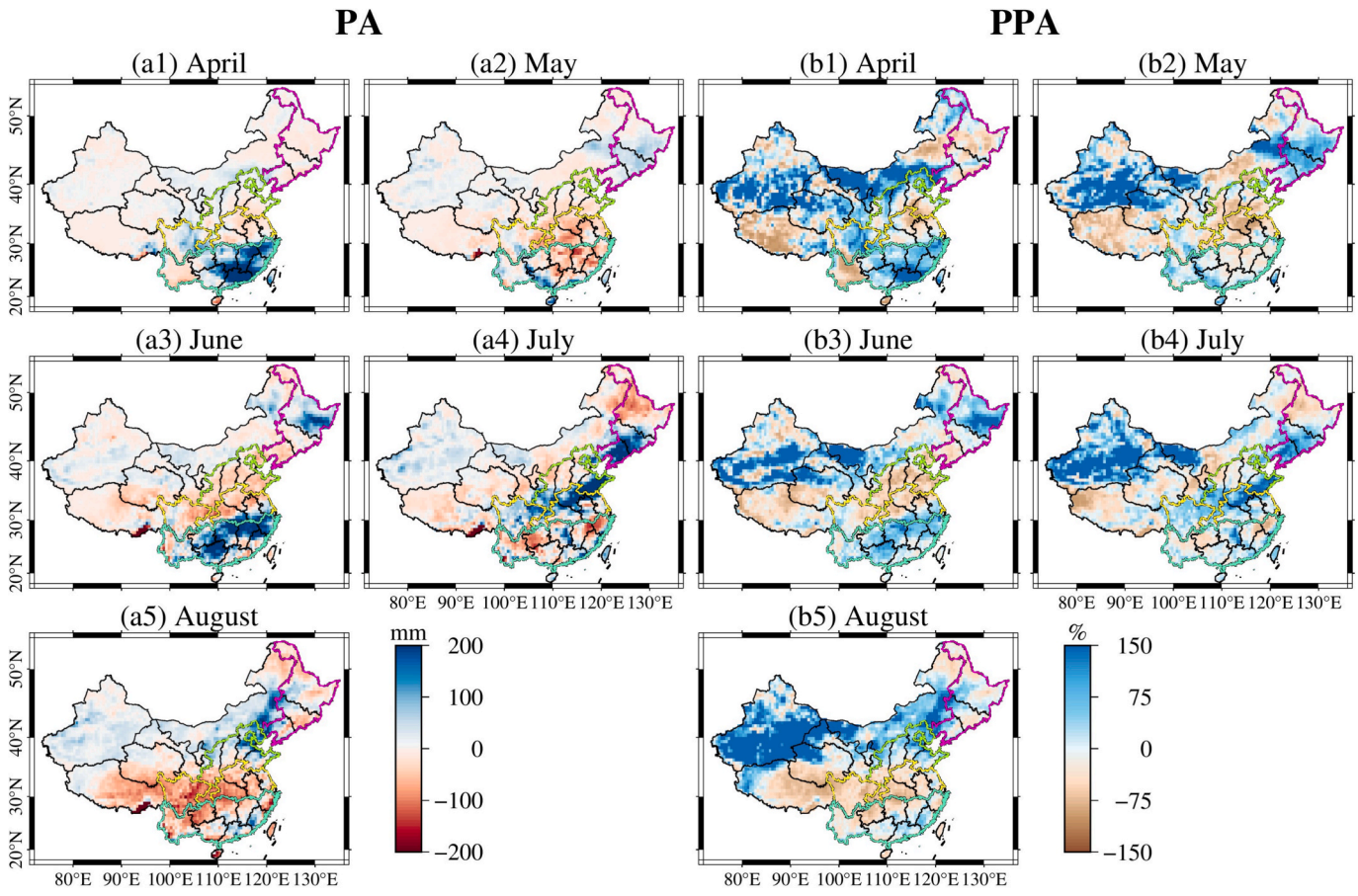

Fig. 2. Spatial distribution of PA and PPA from April to August 2024. Note: Precipitation data for Taiwan Province is available only from 2023 to 2024.

Table 2
PA (mm) and PPA in 20 provinces in eastern China from April to August 2024.

	PA PPA	April	May	June	July	August
Southern China	Guangxi	69.07	46.28	173.58	−5.12	−18.85
		41.90 %	29.16 %	59.04 %	−2.74 %	−5.34 %
	Guangdong	351.90	18.87	24.04	32.79	20.10
		176.69 %	12.13 %	9.52 %	18.09 %	13.48 %
	Yunnan	−19.42	20.29	24.55	−11.99	−38.99
		−46.99 %	20.32 %	12.95 %	−5.38 %	−18.12 %
	Guizhou	38.29	6.21	84.69	−59.05	−83.17
		34.42 %	6.11 %	36.44 %	−29.07 %	−54.15 %
	Hunan	102.78	−47.92	145.57	40.61	−39.37
		55.17 %	−21.63 %	**66.50 %**	32.07 %	−28.79 %
	Jiangxi	189.79	−57.92	154.16	−23.63	−10.64
		87.14 %	−22.10 %	51.61 %	−12.46 %	−9.22 %
	Fujian	157.01	−38.11	84.56	30.34	40.62
		88.59 %	−10.29 %	27.00 %	20.50 %	22.20 %
	Zhejiang	131.17	−29.14	169.40	−43.79	−60.68
		95.03 %	−8.23 %	**76.85 %**	−27.32 %	−30.56 %
Central China	Sichuan	28.52	−3.83	−20.19	53.90	−87.32
		42.29 %	−3.95 %	−13.95 %	28.47 %	−53.17 %
	Hubei	2.67	−57.12	23.93	44.76	−96.10
		1.38 %	−38.23 %	−1.19 %	26.48 %	**−65.39 %**
	Anhui	−0.51	−25.69	52.31	30.97	−53.95
		−14.83 %	−28.46 %	11.23 %	13.52 %	−35.94 %
	Henan	−17.04	−50.90	−37.27	187.02	−47.62
		−36.49 %	−71.25 %	−41.97 %	**104.53 %**	−34.81 %
	Jiangsu	−11.75	−31.61	15.17	65.89	−15.75
		−23.43 %	−42.08 %	1.85 %	28.36 %	−10.13 %
North China	Shaanxi	8.50	−25.82	−35.59	57.04	−16.20
		28.75 %	−38.37 %	−43.59 %	36.89 %	−7.36 %
	Shanxi	7.79	−13.82	−28.22	−8.20	15.45
		34.06 %	−31.53 %	−42.90 %	−5.47 %	14.09 %
	Hebei	8.90	−7.03	−26.91	19.04	89.95
		48.30 %	−20.28 %	−36.45 %	8.91 %	**69.09 %**
	Shandong	−13.94	−18.66	−48.92	227.46	35.72
		−40.28 %	−37.32 %	**−60.06 %**	115.51 %	23.73 %
Northeast China	Liaoning	11.36	15.05	−35.32	175.96	57.70
		53.66 %	28.03 %	−35.55 %	**113.63 %**	55.36 %
	Jilin	−6.88	46.24	−0.83	105.67	4.40
		−23.98 %	**88.39 %**	−0.63 %	**60.75 %**	15.21 %
	Heilongjiang	−4.20	17.45	56.24	−31.38	−3.77
		−18.56 %	32.08 %	**62.14 %**	−21.73 %	−2.76 %

August, the PA values are small positive or negative. Combined with the PPA, it is evident that the increases in precipitation in April and June are more pronounced than the decreases observed in the other months, with noteworthy examples in Guangdong and Fujian. Specifically, the PA is 351.90 mm and the PPA reaches 176.69 % in Guangdong Province (Table 2), leading to severe flooding in April (Du et al., 2025). This prolonged heavy rainfall is primarily associated with the influence of the subtropical high system linked to the El Niño event in 2023 winter, which enhances convective activity in this region (Zhang et al., 2025).

In central China, a contrasting precipitation pattern is observed. In July, positive PA values are recorded in Sichuan (53.90 mm), Hubei (44.76 mm), Anhui (30.97 mm), Henan (187.02 mm), and Jiangsu (65.89 mm) Provinces (Table 2), linked to summer monsoon activity (China Meteorological Administration, 2025). However, during the other four months, precipitation generally falls below the historical average averages in these provinces, indicating drought conditions (Wang et al., 2024b). For instance, PA is −57.12 mm in Hubei Province in May and −87.32 mm in Sichuan Province in August. Notably, Henan Province suffers from persistent precipitation deficits from April to June, with the PPA values of −36.49 %, −71.25 % and −41.97 %. By June 12, meteorological drought conditions in 16 cities across Henan Province had reached severe or higher levels (https://yjglt.henan.gov.cn/2024/06–12/3006879.html). However, the sustained deficits are followed by extreme rainfall in July, where the PPA reaches 104.53 % (Table 2), causing an abrupt alternation from drought to flood (Ministry of Water Resources of the People's Republic of China, 2025). The average precipitation reached 117.2 mm from July 14 to 18 in Henan Province (https://ha.cma.gov.cn/xwzx/xwtt/202407/t20240718_6426724.html). In August, the entire central region experienced relatively dry conditions, primarily due to the abnormally strong westward extension of the subtropical high and the northward shift of the westerly jet stream. These anomalies displaced the rain belt northward, resulting in high temperature and little rain in the region (China Meteorological Administration, 2025).

In part of North China, including Hebei, Shanxi and Shandong Provinces, PA is negative or slightly positive from April to June, indicating a precipitation deficit during spring and early summer (Wang et al., 2024b). However, in July, Shandong Province experiences substantially higher-than-average precipitation, with PA and PPA respectively reaching 227.46 mm and 115.51 % (Table 2), alleviating prior drought conditions but also triggering flood disasters (Department of Emergency Management of Shandong Province, 2025). Similarly, in August, Hebei Province also records large positive anomalies, with PPA reaching 69.09 %.

In Northeast China, PPA increases in Heilongjiang Province in June (62.14 %), but turns negative in July (−21.73 %). In contrast, PPA in Jilin and Liaoning Provinces decrease in June and increase in July. Both provinces experience heavy rainfall in July, with PA values of 105.67

mm and 175.96 mm (Table 2), respectively, causing serious flooding (Ministry of Water Resources of the People's Republic of China, 2025). According to the Liaoning Provincial Meteorological Service, the average precipitation was 193.4 mm, representing a 20 % increase compared to the same period last year (158.8 mm) in July (https://ln.cma.gov.cn/xwzx/qxxw/202308/t20230804_5695338.html). From July to August, the average precipitation reached 433.6 mm in Jilin Province (https://news.cnjiwang.com/jwyc/202501/3915145.html).

3.2. Variations of TWSA and TWF

We analyze the spatial distribution of TWSA and soil moisture storage anomaly (SMSA) in China from April to August, as shown in Fig. 3. In terms of TWSA, the coastal areas of southern China predominantly exhibit positive anomalies. Notably, TWSA in Hubei, Henan, and Anhui Provinces exhibit positive–negative-positive transition over the five-month period, which may indicate a drought flood abrupt alternation in these regions.

The spatial distribution of SMSA and TWSA exhibits certain similarities, potentially reflecting their interrelated roles within the hydrological cycle. However, notable differences also exist. In July, while TWSA in the southern coastal provinces approach zero (Fig. 3a4), SMSA display negative anomalies (Fig. 3b4). This discrepancy may be attributed to extreme climatic events, such as typhoons, which bring heavy precipitation and thus increases TWS (Chen et al., 2020b). Simultaneously, high temperatures in July likely cause elevated evaporation rates, resulting in reduced soil moisture storage (Deng et al., 2024; Meng et al., 2013). In June, TWSA are negative or slightly positive in regions such as eastern Sichuan, Hubei, and Henan Provinces (Fig. 3a3), likely due to continuous drought (Fig. 2a3), high temperatures (National Climate Centre, 2024b), and other factors that exacerbate terrestrial water loss. Nevertheless, the declines in SMSA are not significant in these regions (Fig. 3b3). This can be associated with anthropogenic interventions, such as agricultural irrigation, which may partially offset soil moisture depletion. In addition, uncertainties in the ERA5-Land SMSA data may also contribute to the discrepancy (Zhang et al., 2023).

Fig. 3a6 and b6 present the cumulative distribution functions (CDFs) of TWSA and SMSA from April to August in 2024. Both TWSA and SMSA exhibit numerous high positive and low negative values. This indicates that the intensity and frequency of TWS fluctuations are relatively large during this period.

As mentioned above, TWSA in Hubei and Henan Provinces exhibit pronounced spatial variations, with both positive and negative anomalies. Therefore, the alternation between drought and flood conditions can be intuitively observed. However, in Shandong and Jiangsu Provinces, TWSA does not show significant positive or negative changes over time, despite experiencing considerable fluctuations (Ministry of Water Resources of the People's Republic of China, 2025). This limitation highlights the need for a more precise approach. To address this, TWF can be used to discuss the changes in TWS between two adjacent months, and to more accurately capture regional drought and flood dynamics.

The TWF estimates from April to August 2024 are presented in Fig. 4, which reveals diverse spatiotemporal variation patterns across China. In the Guangdong and Fujian Provinces, the TWF_{MA} (89.79 and 67.42 mm/month) and TWF_{JM} (29.19 and 30.31 mm/month) are positive or

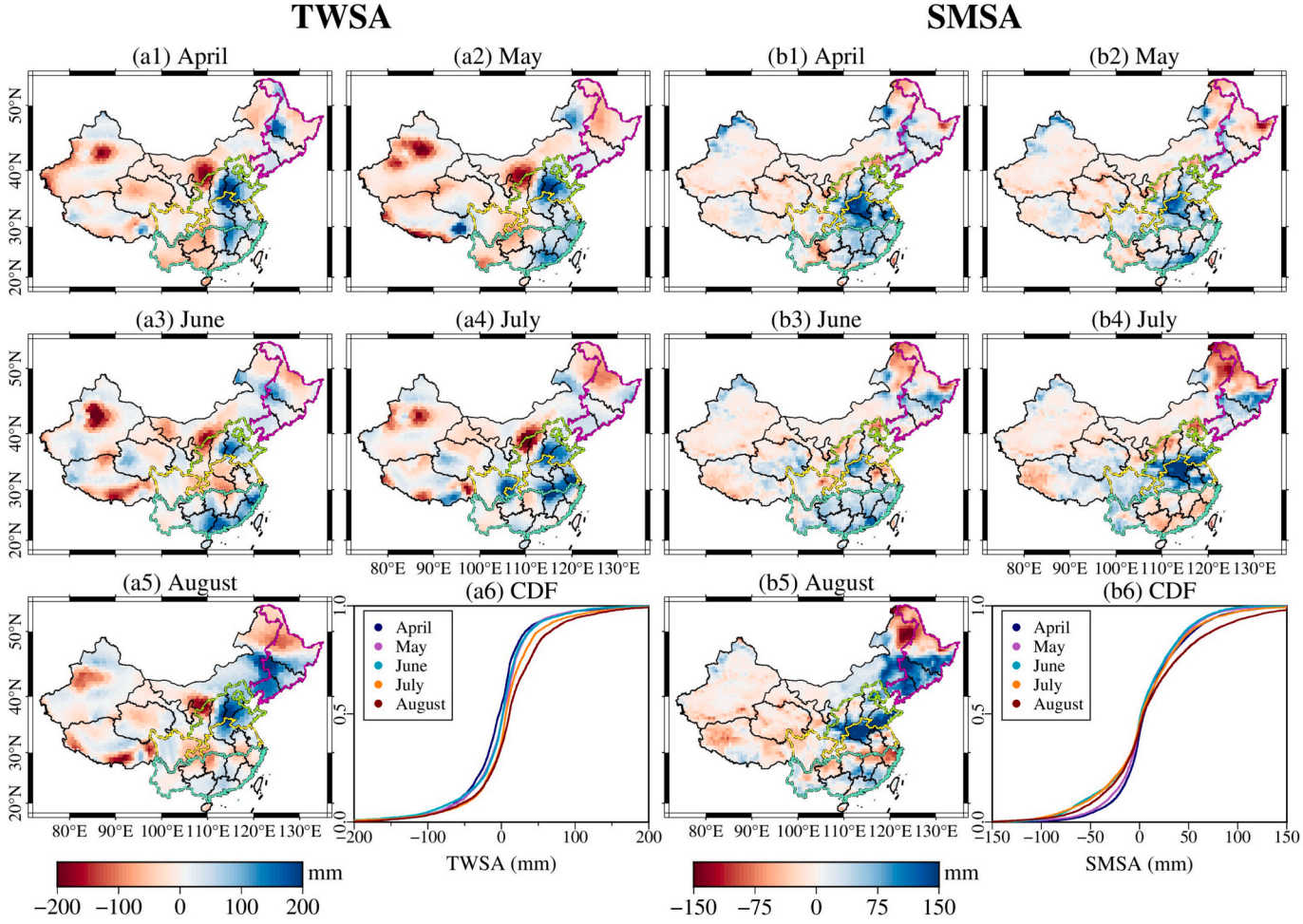

Fig. 3. Spatial distribution of TWSA, SMSA and their CDFs from April to August 2024.

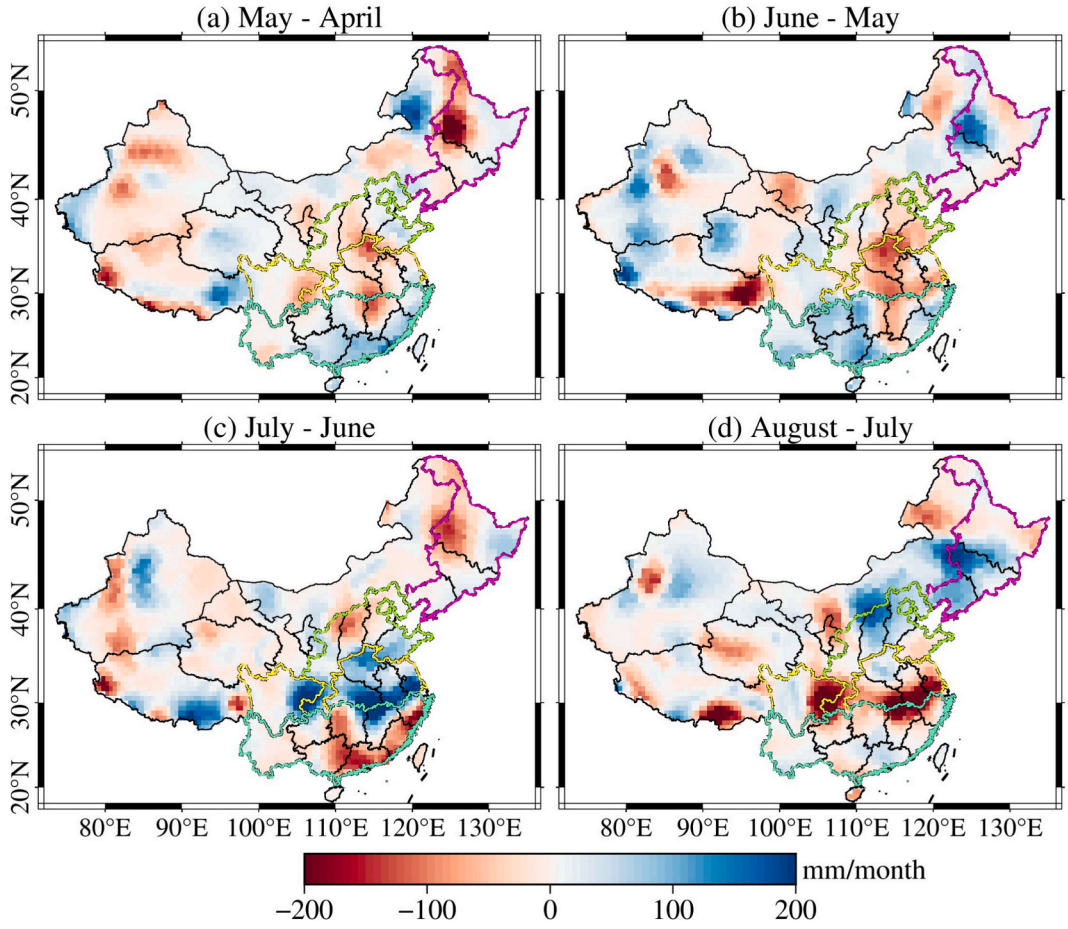

Fig. 4. Spatial distribution of TWF during May − April (TWF_{MA}), June − May (TWF_{JM}), and July- June (TWF_{JJ}), August − July (TWF_{AJ}) in 2024.

slightly negative, reflecting the influence of heavy rainfall events between April and June (Liu et al., 2025). In contrast, TWF_{JJ} (−108.74 and −91.59 mm/month) exhibit pronounced negative fluxes (Table 3), which are consistent with a sharp decline in TWSA in July (Fig. 3a3 and a4), underscoring significant water storage loss in these regions.

In central China, the TWF_{MA} exhibits negative or slightly positive in certain local areas, such as eastern Sichuan Province and the border regions of Hubei Province and Jiangxi, which corresponds to a reduction in TWSA in most areas. The TWF_{JM} indicates intensification of TWS deficits in the central provinces. Notably, TWF_{JJ} reveals substantial positive fluxes. For instance, the TWF_{JJ} in Hubei Province reaches 129.64 mm/month (Table 3), with a maximum grid value of 336.23 mm/month. This is primarily attributed to the TWS deficit caused by drought in June, followed by heavy rainfall that results in a large positive TWSA in July. Together, these changes indicate a rapid transition from drought to flood (Xinhua News, 2024b). However, the TWF_{AJ} declines sharply to −93.31 mm/month. Combined with the negative TWSA in August (Fig. 3a5), this reflects that Hubei Province experiences a transition from flood to drought (Department of Emergency Management of Hubei Province, 2024).

In Shandong and Hebei Provinces, TWSA remains largely positive in April and May, with corresponding TWF_{MA} of 7.14 and 12.74 mm/month. However, due to reduced precipitation in June (Fig. 2a3), TWF_{JM} (−54.76 and −29.22 mm/month) turn negative. Subsequently, TWF_{JJ} (60.19 and −6.51 mm/month) and TWF_{AJ} (−15.50 and 61.29 mm/month) increase from south to north (Table 3), indicating that Shandong and Hebei Provinces successively undergo a transition from drought to flood (Department of Emergency Management of Shandong Province, 2025; Hebei Meteorological Service, 2025).

In Northeast China, particularly in western Heilongjiang Province, TWF_{MA} is markedly negative, with a maximum grid value of −237.27 mm/month. This results from a sudden transition in TWSA, which changes from positive in April to negative in May (Fig. 3a1 and a2), highlighting the severe drought risks in May. As local climate conditions slightly moderate, TWF_{JM} in western Heilongjiang Province turns positive, indicating a partial alleviation of drought stress in June. Meanwhile, the TWF_{AJ} in Liaoning and Jilin Provinces reach 91.62 and 90.51

Table 3
TWF (mm) in 20 provinces in eastern China from April to August 2024.

		TWF_{MA}	TW_{JM}	TWF_{JJ}	TWF_{AJ}
Southern China	Guangxi	49.37	77.04	−53.95	−3.15
	Guangdong	89.79	29.19	−108.74	18.47
	Yunnan	−3.96	40.96	−3.29	5.83
	Guizhou	5.88	66.12	−0.44	−34.67
	Hunan	5.18	26.56	−24.58	−17.64
	Jiangxi	−38.59	−45.79	92.70	−97.56
	Fujian	67.42	30.31	−91.59	−5.57
	Zhejiang	33.77	8.56	−55.68	−46.49
Central China	Sichuan	−9.96	12.93	46.14	−46.09
	Hubei	−31.78	−58.52	129.64	−93.31
	Anhui	−19.92	−51.94	114.50	−119.46
	Henan	−55.96	−97.31	93.68	23.09
	Jiangsu	−0.44	−22.18	91.73	−85.20
North China	Shaanxi	−6.27	−5.08	14.09	−4.67
	Shanxi	−32.13	−23.55	−34.75	95.91
	Hebei	12.74	−29.22	−6.51	61.29
	Shandong	7.14	−54.76	60.19	−15.50
Northeast China	Liaoning	2.20	3.37	8.79	91.62
	Jilin	−15.91	26.16	−6.75	90.51
	Heilongjiang	−48.98	33.24	−23.95	13.79

mm/month (Table 3), respectively, primarily driven by the heavy rainfall in August.

In summary, the analysis of TWF provides critical insights into the spatiotemporal dynamics of extreme hydrological events and transitions between drought and flood conditions in 2024. These results demonstrate that TWF is an important indicator for capturing TWS variations and for assessing the processes and impacts of hydrological extremes across China.

3.3. The percentages and maximum of TWF

To better highlight the extreme characteristics of TWSA changes in 2024, we calculate the percentiles of TWF and |TWF| (i.e., the absolute value of TWF) for four different periods in the historical record (2002–2024). Fig. 5a presents the spatial distribution of TWF percentiles. Across most regions of China, TWF values fall within the extreme percentile ranges (either below the 10th or above the 90th percentile) during these four periods. Statistically, 36.52 %, 46.22 %, 44.79 %, and 46.48 % of grids all into these categories for their respective periods (Fig. 5c1). This suggests that the intensity of TWSA variations observed in 2024 is historically elevated. To further identify where these historically high TWSA fluctuations occur, we analyze the spatial distribution of |TWF| percentiles (80th – 100th), which captures the magnitude of TWSA changes (Fig. 5b). Regions exhibiting significant changes in TWSA in 2024 include Guangdong, eastern Guangxi, eastern Sichuan, Hubei, Anhui, Henan, northern North China, Liaoning, Jilin, and northern and western Heilongjiang.

Additionally, we analyze the years and months in which the maximum values of |TWF|, |PA| and |SMF| occur during the 2002–2024 period (Fig. 6). The results reveal a notable similarity of |PA| and |TWF| maximum in the past six years, with 55.97 % and 74.84 % of the grids reaching their peak values during this period. Moreover, the proportion of grid with the maximum |TWF| has shown an increasing trend over the past six years, with 2024 (19.89 %), 2023 (18.38 %), and 2020 (12.01 %) being the top three years. A similar pattern is observed for |PA|, where 2024 (18.77 %), 2020 (10.66 %), and 2023 (8.76 %) also represent the peak years. These findings indicate that hydrological and precipitation anomalies have become more extreme in recent years, particularly in 2024.

In terms of spatial distribution, the years with the maximum values of |TWF| and |PA| in regions such as Jiangxi, Hubei, and Anhui Provinces are mostly concentrated in 2019–2021. In contrast, maximum values in northwest China are primarily concentrated in 2022–2024. Differences are also observed in the statistics of months with the

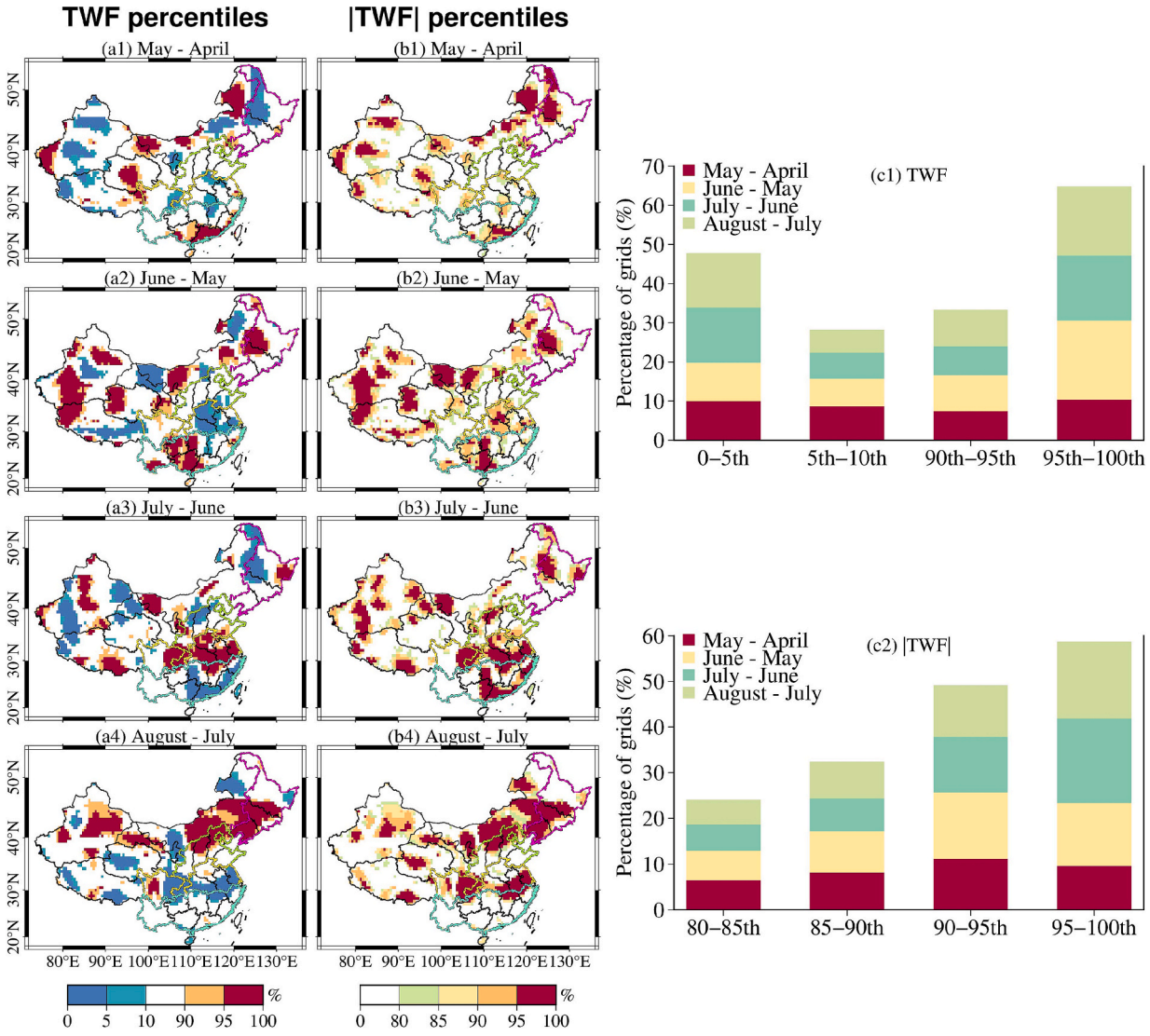

Fig. 5. The percentiles of TWF and |TWF| for four different periods from April to August in 2024 relative to the whole TWF estimates. a-b: spatial distribution; c: percentage of grids.

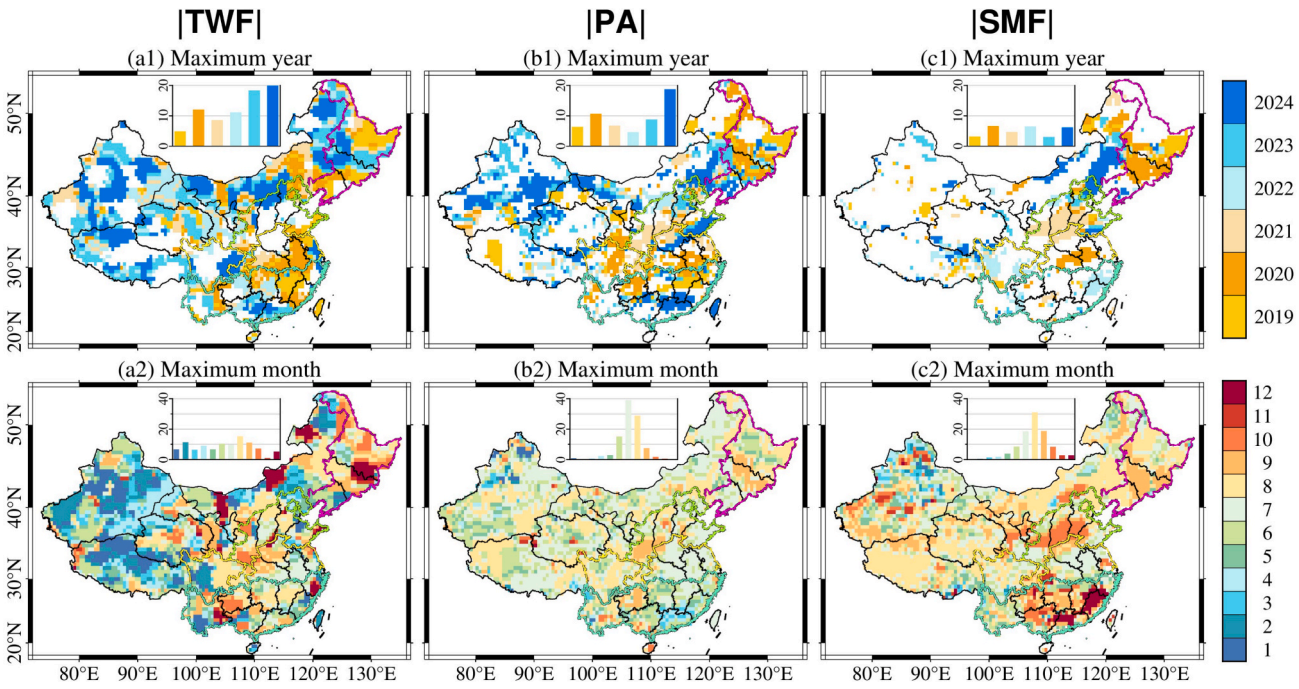

Fig. 6. Spatial distribution of the years and months in which the maximum values of |TWF|, |PA|, and |SMF| occur across China during 2002 – 2024 period. Embedded bar charts show the percentage of grids with maximum values for each year or month.

maximum values. The high proportions for |TWF| and |PA| are concentrated from June to September, accounting for 46.40 % and 90.72 % of the total grids. However, |TWF| also exhibits a relatively high proportion in winter (January, February, and December), accounting for 23.34 %, whereas |PA| is only 1.20 %.

The Fig. 6a2 show that regions with maximum |TWF| values in winter are primarily located in western high-altitude regions and northern high-latitude areas. This pattern is largely due to China's geographical location, which determines its precipitation characteristics—rainfall is concentrated in summer, with limited precipitation in the northwest. Furthermore, low temperatures in winter result in shorter precipitation retention times in these regions, making snowfall anomalies a more significant contributor to changes in TWS. This explains the spatial difference in the monthly maximum values of |PA| and |TWF|.

There is a notable spatial consistency between |SMF| and |PA|, particularly in regions such as Hubei Province, Anhui Province, North China, Jilin Province, and southeastern Heilongjiang Province. These regions exhibit either consistency or lag in the distribution of months with maximum values, which may reflect differences in various hydrological processes responding to climate change. Statistically, the high monthly proportions of |SMF| are concentrated between June and October, while the top years are 2020, 2022, and 2024. Overall, the consistency between |SMF| and |TWF| is weaker than that between |TWF| and |PA|.

4. Discussion

4.1. Uncertainties in TWF estimations

The GRACE/GRACE-FO mission estimates the changes of TWS by monitoring dynamic variations in the earth's gravity field. Before generating the gravity field data products used in this study, the original GRACE/GRACE-FO data undergo processing to reduce measurement errors and noise. However, this process faces many challenges. First, signal leakage and stripe noise may occur during the inversion of gravity field data (Swenson and Wahr, 2006). Although CSRM data are widely used in hydrological research, their inherent errors and uncertainties still need to be considered. In this study, TWSA is used to calculate TWF, which may transfer inherent errors to TWF, resulting in reduced accuracy of the results. We discuss the impact of the inherent errors on the TWF changes in detail in Section 4.2.

Second, as mentioned earlier, an 11-month data gap exists between the GRACE and GRACE-FO missions. The 32-day threshold is determined based on statistical results to limit the time interval of CSRM when calculating TWF, which also may introduce additional uncertainties on TWF and further affect our results. In addition, the data coverage of GRACE satellites, launched in 2002, spans only from 2002 to the present. This temporal limitation hinders long-term estimates over past multi-decadal timescales. In the future, we can attempt to reconstruct data to fill the gaps in the past and supplement the data for missing months (Humphrey and Gudmundsson, 2019; Li et al., 2023). This will allow us to quantify the characteristics of TWF changes in a longer time series and improve the reliability of the estimates.

Furthermore, monthly TWSA and SMSA are both monthly mean data, while TWF and SMF are the differences of TWSA and SMSA in two adjacent months, respectively. However, PA is the anomaly value calculated from the monthly cumulative precipitation and quantifies the deviation of each monthly precipitation from the average monthly precipitation of the same period. In contrast, TWSA reflects the deviation from the long-term mean. These discrepancies will introduce certain uncertainties in the results when comparing the spatial distribution of the maximum values (Fig. 6).

4.2. A conservative assessment of TWF variation in 2024 considering potential GRACE-FO errors

Although the GRACE-FO mission has made significant advancements in data quality and scientific applications compared to the GRACE mission (Kornfeld et al., 2019), it is still affected by various factors that can introduce data errors. These include the solar activity cycle (Landerer et al., 2020; Park et al., 2023), attitude and orbit control system leakage (Cossavella et al., 2022), accelerometer calibration error (McCullough et al., 2020), etc. To analyze the possible increased errors contributing to GRACE-FO TWSA and further to TWF estimates in 2024,

we adjust the TWF values during GRACE-FO by ± 2 cm (adding 2 cm when TWF < 0 and subtracting 2 cm when TWF > 0), then recalculate the TWF and |TWF| percentiles for 2002–2024 in four different periods, i.e. TWF_{MA}, TWF_{JM}, TWF_{JJ} and TWF_{AJ}.

The results indicate that TWF and |TWF| percentiles have small grids percentage change after the 2 cm error adjustment (Fig. 7). The percentage of grids within the extreme percentile ranges of TWF (0-10th and 90-100th) and |TWF| (80-100th) have mostly decreased. Specifically, TWF percentiles in the four periods respectively decrease by 12.82 %, 12.30 %, 9.28 %, and 13.26 %, within these extreme percentile ranges. And |TWF| percentiles respectively decrease 12.58 %, 12.56 %, 8.71 % and 12.37 %. From a spatial distribution perspective, the regions exhibiting significant changes before and after error adjustment are predominantly located in western China, including Xinjiang Uygur Autonomous Region, Xizang Autonomous Region, and Qinghai Province, although these areas are not the primary focus of this study. In conclusion, the possible increased errors of GRACE-FO TWSA have a limited impact on overall TWF estimates, and will not alter our conclusions.

4.3. Intensified variability in TWF driven by precipitation

As shown in Fig. 8b, the STD of TWF_{CSRM} (STD_{TWF}) is greater in the GRACE-FO period than in the GRACE period for 19 of the 20 selected provinces, except for Shandong Province. The IQR of TWF_{CSRM} (IQR_{TWF}) shows a similar pattern (Fig. 8d), being larger in the GRACE-FO period for 16 provinces. These suggest that TWF fluctuations are generally more pronounced in the GRACE-FO period. Therefore, we suppose the primary driver of the differences in TWF variability is precipitation changes between the two periods.

To demonstrate this speculation, this study first reconstructs the TWSA from 2002 to 2024 using the precipitation and temperature data, with the CSRM in the GRACE period serving as a constraint for calibration. Since TWF_{REC} is calibrated using TWSA in the GRACE period, the errors associated with the GRACE-FO satellites are excluded. It helps to reduce reconstruction biases caused by differences in the quality of satellite observation data and minimize the comparison bias caused by differences in the changes in the original signal between the two periods (Hacker and Kusche, 2024). The contribution of precipitation can then be assessed by comparing the normalized MAD between TWF_{REC} and TWF_{CSRM} (i.e. TWF_{MADR} and TWF_{SMAD}) in the two periods.

As shown in Fig. 8a, TWF_{MADR} in the GRACE period is smaller for 9 provinces (Guangxi, Guizhou, Hunan, Sichuan, Zhejiang, Shaanxi, Shanxi, Shandong, and Heilongjiang Provinces) than the values in the GRACE-FO period. Additionally, TWF_{MADR} in the two periods only exhibit slight differences. Except for Sichuan Province (0.13), the differences of TWF_{MADR} in the other provinces range from 0.02 to 0.09. TWF_{SMAD} (Fig. 8c) differs from TWF_{MADR}: it is larger in the GRACE-FO period for 10 provinces, and the range of differences between the two periods is relatively wider (0.01–0.21). Importantly, 9 provinces (Guangxi, Jiangxi, Fujian, Sichuan, Hubei, Henan, Shanxi, Hebei, and Heilongjiang Provinces) exhibit consistent the period to period ranking for both TWF_{SMAD} and TWF_{MADR}, confirming the robustness of our normalized MAD metrics. Nevertheless, TWF_{SMAD} still effectively reflects the explanatory power of precipitation for TWF fluctuations. Combined with the STD_{TWF} (Fig. 8b) and IQR_{TWF} (Fig. 8d), these indicate that the MAD between the TWF_{REC} and the TWF_{CSRM} is generally greater in the GRACE-FO period, which can partially explain the contribution of precipitation to the increased TWF variability.

Then, we compare the PA fluctuations between the two periods for each province (Fig. 8b and d). For most provinces, both STD_{PA} and IQR_{PA} are larger in the GRACE-FO period, which are consistent with the STD_{TWF} and IQR_{TWF}. This consistency suggests that the widespread intensification of TWF fluctuations may be jointly driven by enhanced seasonal precipitation variability and more frequent extreme precipitation events. However, STD_{PA} is smaller in the GRACE-FO period, contrasting with the STD_{TWF} in Guangxi and Fujian Provinces. By examining the PA time series for these provinces (not shown), we find that some large PA values occur in the GRACE period, and the missing TWF data fails to reflect the corresponding TWS changes driven by extreme precipitation. Thus, the STD_{TWF} is likely underestimated in the GRACE period.

In Shandong Province, the STD_{PA} is significantly higher in the GRACE-FO period, while the STD_{TWF} exhibits the opposite trend. This suggests that TWS fluctuates more dramatically in Shandong Province in the GRACE period. Based on the TWSA time series for the province (not shown), we attribute this phenomenon to differences in the frequency and intensity of extreme climate events between the two periods. During the GRACE period, Shandong Province has experienced fewer but more intense extreme events, such as the severe drought in 2002 (Zhang et al., 2004) and the catastrophic flood in 2012 (Qiu et al., 2022). These high-intensity events cause substantial deviations in TWS from its mean state, leading to higher STD_{TWF} during the GRACE period. In contrast, fluctuations in TWS occur more frequently, but their amplitudes are relatively smaller, resulting in a lower STD_{TWF} in the GRACE-FO period. After removing the influence of extremes, IQR_{TWF} becomes larger

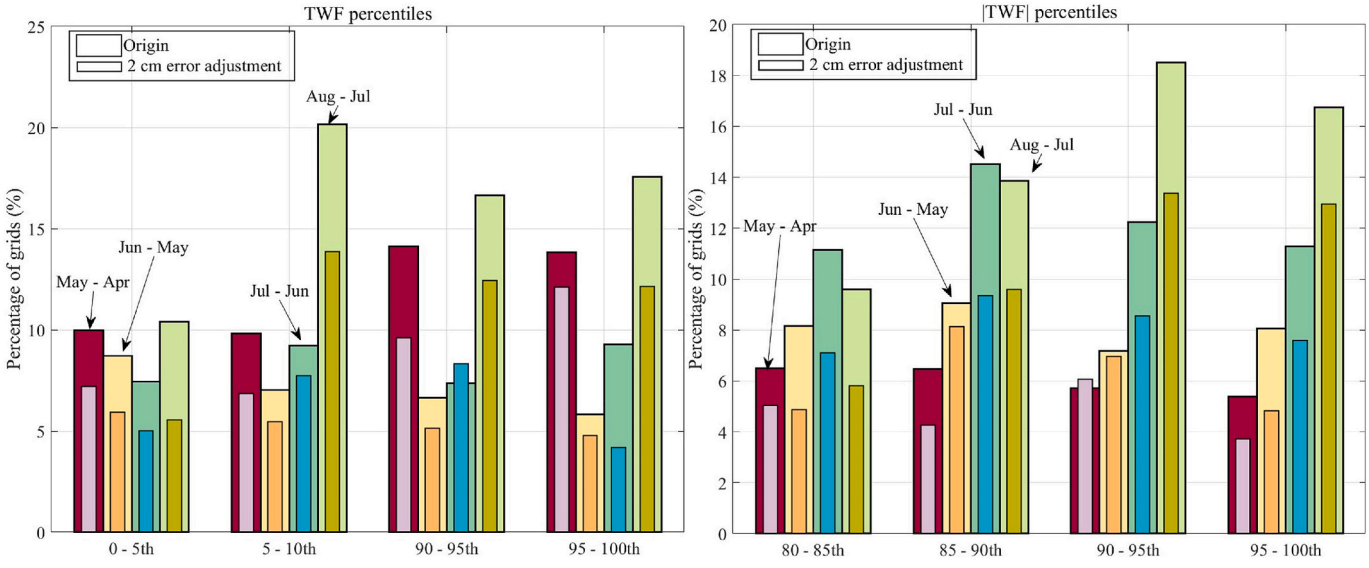

Fig. 7. The percentage of grids of TWF and |TWF| percentiles before and after the 2 cm error adjustment for four different periods from April to August in 2024.

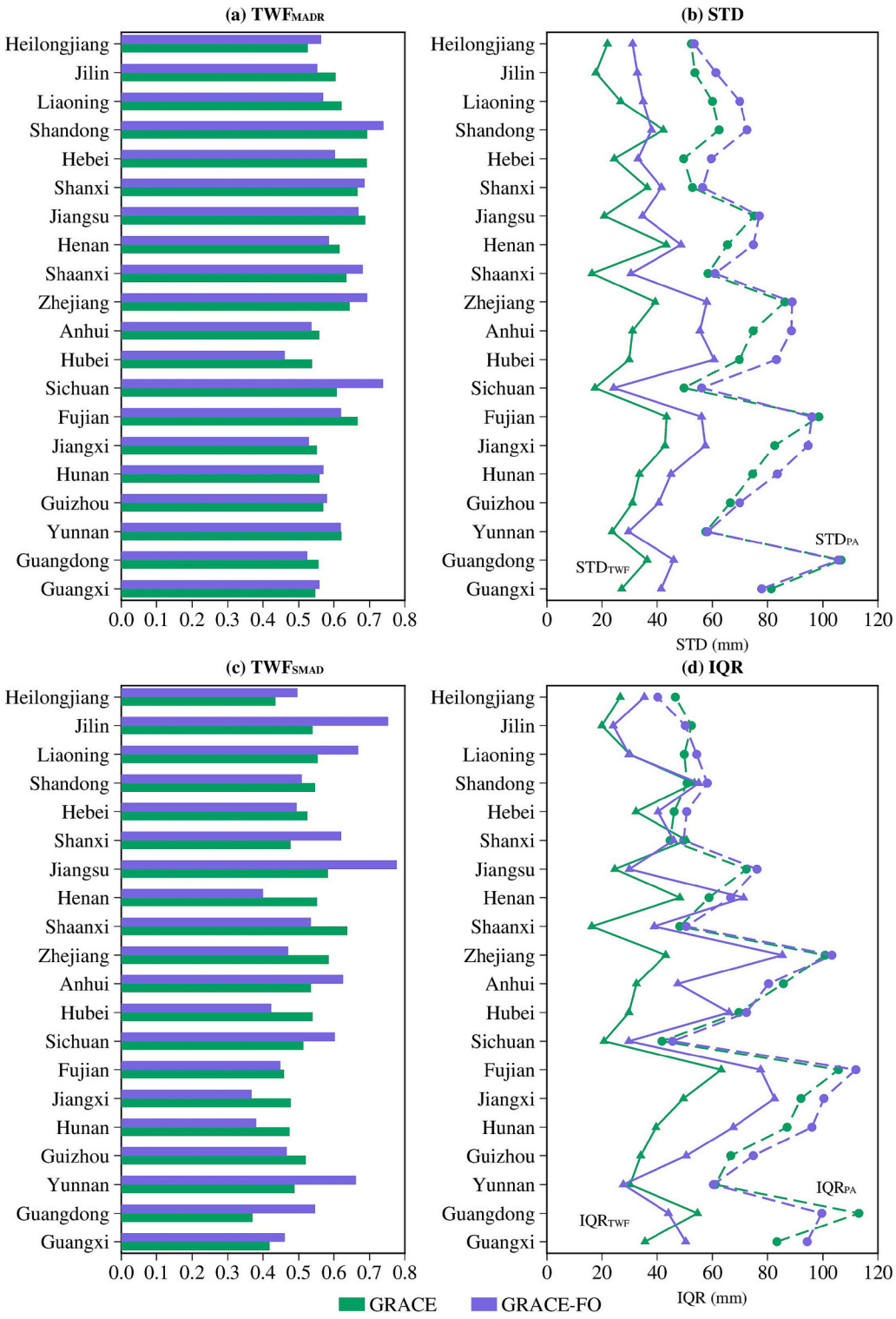

Fig. 8. Comparison of the TWF_{MADR}, STD_{TWF}, STD_{PA}, TWF_{SMAD}, IQR_{TWF} and IQR_{PA} in 20 selected provinces in the GRACE and GRACE-FO period. For a better view, STD_{PA} and IQR_{PA} have been respectively moved 30 mm to the right. (a) TWF_{MADR}. (b) STD_{TWF} and STD_{PA}. (c) TWF_{SMAD}. (d) IQR_{TWF} and IQR_{PA}.

relative to STD_{TWF}, with IQR_{TWF} being even greater in the GRACE-FO period. This indicates that the variability of TWF after removing extreme values is more intense in the GRACE-FO period, leading to a wider range of stable TWF fluctuations. Additionally, climate change and human activities, particularly groundwater extraction, are crucial factors influencing TWS variations. These factors have different impacts on TWSA in Shandong Province in the two periods, further contributing to the differences in TWF variability.

4.4. Comparison with global regions with the same latitude

As a key driver of disaster risks, climate change has inflicted substantial losses on nations worldwide (World Meteorological Organization, 2024). Thus, enhancing disaster risk prediction, planning, and resilience building is critical for global sustainability (United Nations, 2015). This study employs TWF as an indicator to quantify extreme climate change, which has been effectively verified in China.

Subsequently, we take the contiguous United States as a representative case outside China for comparative analysis to provide a global perspective on the effectiveness of TWF applications. As shown in Fig. 9, the year and month with the maximum value of |TWF| in the contiguous United States aligns with the conclusions in China: 66.82 % of grid maxima occur within the past six years, exhibiting an upward trend. The top three years with the highest proportions are 2021 (15.98 %), 2023 (13.88 %), and 2024 (12.88 %). Specifically, the 2021 southwestern U.S. drought (Mankin et al., 2021), the alternating drought-flood events in western states (e.g., California and Nevada) during 2022–2023 (Smith, 2024) and the 2024 tornado-induced TWSA changes (Smith, 2025) all corresponded to extreme TWF signals. These findings validate the universality of TWF across diverse climatic zones. Future research can expand to global scales by integrating regional disaster databases with socioeconomic metrics, thereby providing scientific support for national disaster risk reduction policies.

5. Conclusion

In 2024, China experiences frequent and severe extreme hydrological events, leading to significant changes in TWSA. To analyze these changes, this study defines TWF based on GRACE/GRACE-FO data, enabling quantification of monthly-scale TWSA fluctuations from April to August 2024. By integrating TWF with precipitation data, we further investigate the underlying driving mechanisms behind the increased variability of TWF.

This study shows pronounced spatiotemporal variations in TWSA across China in 2024, which are similar to the changes in PA and PPA. This indicates that change in precipitation pattern is a predominant factor affecting the changes in TWSA. From a long-term perspective (2002–2024), 36.52 %, 46.22 %, 44.79 %, and 46.48 % of grids fall into the extreme TWF percentile ranges (below the 10th or above the 90th) in the four periods (May − April, June − May, July − June, and August − July). And 74.84 % of grids reach their maximum |TWF| during 2019–2024, of which 19.89 % are observed in 2024. These results confirm that TWF is historically extreme in most parts of China in 2024, further emphasizing the severity of hydrological fluctuations. Further investigation of the drivers behind these extremes indicates that STD_{PA}, IQR_{PA}, STD_{TWF} and IQR_{TWF} are more pronounced in the GRACE-FO period, suggesting that the intensification of TWF fluctuations is primarily driven by increased precipitation variability.

This study provides robust observational evidence of intensifying hydrological extremes in China under climate change. It emphasizes the severity of extreme hydrological events in China in 2024 and demonstrates the utility of TWF in capturing short-term hydroclimatic fluctuations and in assessing regional water storage responses. However, limitations remain, including uncertainties in TWF estimates derived from GRACE/GRACE-FO data due to data gaps and signal noise. Future studies should integrate multi-source datasets to enhance data reconstruction and extend the analysis to other climate-sensitive regions to better understand the broader implications of hydroclimatic extremes on water resources.

CRediT authorship contribution statement

Yulong Zhong: Writing – review & editing, Writing – original draft, Methodology, Funding acquisition, Formal analysis, Conceptualization. **Jingwen Zhou:** Writing – original draft, Visualization, Formal analysis, Data curation, Conceptualization. **Baoming Tian:** Writing – review & editing. **Guodong Xu:** Writing – review & editing. **Yunlong Wu:** Writing – review & editing, Resources, Funding acquisition.

Declaration of competing interest

The authors declare that they have no known competing financial interests or personal relationships that could have appeared to influence the work reported in this paper.

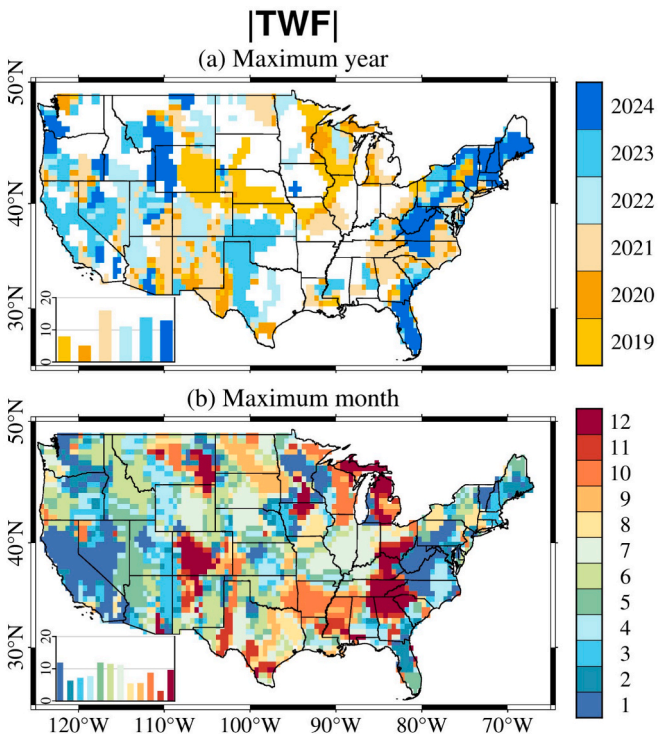

Fig. 9. Spatial distribution of the years and months in which the maximum values of |TWF| occur in the contiguous United States during 2002 – 2024 period. Embedded bar charts show the percentage of grids with maximum values for each year or month.

Acknowledgments

This work is funded jointly by the Natural Science Foundation of China (Grants Nos. 42374032 and 42442015), the China Scholarship Council (202306410033), and the Key Laboratory of Natural Resources Monitoring and Supervision in Southern Hilly Region, Ministry of Natural Resources (NRMSSHR2024Z02).

Data availability

The CSRM RL06.3 datasets can be downloaded in https://www2.csr.utexas.edu/grace/RL06_mascons.html. The CHM_PRE data can be downloaded in https://www.tpdc.ac.cn/zh-hans/data/e5c335d9-cbb9-48a6-ba35-d67dd614bb8c. CLDAS-V2.0 data can be downloaded in https://data.cma.cn/data/cdcdetail/dataCode/NAFP_CLDAS2.0_NRT.html. The ERA5-Land data can be available in https://cds.climate.copernicus.eu/datasets/reanalysis-era5-land-monthly-means?tab=overview.

References

Chen, H., Wang, S., Zhu, J., Zhang, B., 2020a. Projected changes in abrupt shifts between dry and wet extremes over China through an ensemble of regional climate model simulations. J. Geophys. Res. Atmos. 125.

Chen, J.L., Wilson, C.R., Tapley, B.D., Yang, Z.L., Niu, G.Y., 2009. 2005 drought event in the Amazon River basin as measured by GRACE and estimated by climate models. J. Geophys. Res. Solid Earth 114.

Chen, W., Zhong, M., Feng, W., Zhong, Y., Xu, H., 2020b. Effects of two strong ENSO events on terrestrial water storage anomalies in China from GRACE during 2005-2017. Chin. J. Geophys. 63, 141–154.

China Meteorological Administration, 2024. Blue Book on Climate Change in China (2024). Science Press, Beijing.

China Meteorological Administration, 2024b. China Meteorological Administration Land Data Assimilation System.

China Meteorological Administration, 2025. China Climate Bulletin (2024).

Cossavella, F., Herman, J., Hoffmann, L., Fischer, D., Save, H., Schlepp, B., Usbeck, T., 2022. Attitude control on GRACE Follow-on: experiences from the first years in orbit. In: Cruzen, C., Schmidhuber, M., Lee, Y.H. (Eds.), Space Operations: beyond Boundaries to Human Endeavours. Springer International Publishing, Cham, pp. 493–517.
Deng, H., Li, Y., Zhang, Y., Chen, X., 2024. Monitoring spatio-temporal variations of terrestrial water storage changes and their potential influencing factors in a humid subtropical climate region of Southeast China. J. Hydrol. 634.
Department of Emergency Management of Hubei Province, 2024. Analysis report on natural disaster risk situation in Hubei Province in September 2024.
Department of Emergency Management of Shandong Province, 2025. Basic situation of natural disasters in Shandong Province in 2024.
Ditmar, P., 2018. Conversion of time-varying Stokes coefficients into mass anomalies at the Earth's surface considering the Earth's oblateness. J. Geod. 92, 1401–1412.
Domrös, M., Peng, G., 2012. The Climate of China. Springer Science & Business Media.
Du, H., Hu, Y., Li, Z., Wang, M., Zhuang, Y., 2025. Characteristics of climate anomalies and major weather and climate events in Guangdong Province in 2024. Guangdong Climate Center 47, 1–5.
Duan, A., Zhong, Y., Xu, G., Yang, K., Tian, B., Wu, Y., Bai, H., Hu, E., 2024. Quantifying the 2022 extreme drought in the Yangtze River Basin using GRACE-FO. J. Hydrol. 630.
Eicker, A., Forootan, E., Springer, A., Longuevergne, L., Kusche, J., 2016. Does GRACE see the terrestrial water cycle "intensifying"? J. Geophys. Res. Atmos. 121, 733–745.
Famiglietti, J.S., Rodell, M., 2013. Water in the balance. Science 340, 1300–1301.
Fischer, E.M., Sippel, S., Knutti, R., 2021. Increasing probability of record-shattering climate extremes. Nat. Clim. Chang. 11, 689–695.
Gerdener, H., Engels, O., Kusche, J., 2020. A framework for deriving drought indicators from the Gravity Recovery and climate Experiment (GRACE). Hydrol. Earth Syst. Sci. 24, 227–248.
Hacker, C., Kusche, J., 2024. How realistic are multi-decadal reconstructions of GRACE-like total water storage anomalies? J. Hydrol. 645, 132180.
Han, J., Miao, C., Gou, J., Zheng, H., Zhang, Q., Guo, X., 2022. A new daily gridded precipitation dataset for the Chinese mainland based on gauge observations. Earth Syst. Sci. Data 15, 3147–3161.
Hebei Meteorological Service, 2025. Top ten weather and climate events in Hebei Province in 2024.
Humphrey, V., Gudmundsson, L., 2019. GRACE-REC: a reconstruction of climate-driven water storage changes over the last century. Earth Syst. Sci. Data 11, 1153–1170.
IPCC, 2023. Climate change 2023: Synthesis Report, Geneva, Switzerland.
Kornfeld, R.P., Arnold, B.W., Gross, M.A., Dahya, N.T., Klipstein, W.M., Gath, P.F., Bettadpur, S., 2019. GRACE-FO: the gravity recovery and climate experiment follow-on mission. J. Spacecr. Rocket. 56, 931–951.
Lai, Y., Zhang, B., Yao, Y., 2025. Investigating the historic drought in the Yangtze River Basin in 2022–2023 by jointly using GRACE, land surface models, and drought index. J. Hydrol.: Reg. Stud. 58.
Lan, C.W., Lo, M.H., Chou, C., Kumar, S., 2016. Terrestrial water flux responses to global warming in tropical rainforest areas. Earth's Future 4, 210–224.
Landerer, F.W., Flechtner, F.M., Save, H., Webb, F.H., Bandikova, T., Bertiger, W.I., Bettadpur, S.V., Byun, S.H., Dahle, C., Dobslaw, H., Fahnestock, E., Harvey, N., Kang, Z., Kruizinga, G.L.H., Loomis, B.D., McCullough, C., Murböck, M., Nagel, P., Paik, M., Pie, N., Poole, S., Strekalov, D., Tamisiea, M.E., Wang, F., Watkins, M.M., Wen, H.Y., Wiese, D.N., Yuan, D.N., 2020. Extending the global mass change data record: GRACE Follow-On instrument and science data performance. Geophys. Res. Lett. 47.
Li, Q., Liu, X., Zhong, Y., Wang, M., Bai, H., Xiao, C., 2023. Assessing the interannual and subseasonal variabilities in water storage using multi-source soil moisture products and GRACE/GRACE-FO satellites and its applications. J. Hydrol. 627, 130439.
Liu, S., Wu, Y., Xu, G., Xiao, C., Wu, X., Zhong, Y., 2025. Revealing the spatiotemporal evolution of the 2024 extreme flood in Guangdong Province: Insights from GRACE-FO and in situ measurements. J. Hydrol.: Reg. Stud. 59.
Long, D., Longuevergne, L., Scanlon, B.R., 2014. Uncertainty in evapotranspiration from land surface modeling, remote sensing, and GRACE satellites. Water Resour. Res. 50, 1131–1151.
Long, D., Scanlon, B.R., Longuevergne, L., Sun, A.Y., Fernando, D.N., Save, H., 2013. GRACE satellite monitoring of large depletion in water storage in response to the 2011 drought in Texas. Geophys. Res. Lett. 40, 3395–3401.
Mankin, J.S., Simpson, I., Hoell, A., Fu, R., Lisonbee, J., Sheffield, A., Barrie, D., 2021. NOAA Drought Task Force Report on the 2020–2021 Southwestern U.S. Drought, in: IV, N.D.T.F., National Integrated Drought Information, S., Modeling, A.P., Projections, P. (Eds.).
McCullough, C.M., Harvey, N., Save, H., Bertiger, W., Miller, M.A., Landerer, F.W., 2020. Improvements in GRACE-FO accelerometer modeling and calibrations, AGU Fall Meeting Abstracts, pp. G001-003.
Meng, L., Long, D., Quiring, S.M., Shen, Y., 2013. Statistical analysis of the relationship between spring soil moisture and summer precipitation in East China. Int. J. Climatol. 34, 1511–1523.
Ministry of Emergency Management of the People's Republic of China, 2025. Basic Situation of Natural Disasters in China in 2024.
Ministry of Water Resources of the People's Republic of China, 2025. China Flood and Drought Disaster Prevention Bulletin 2024. China Water and Power Press.
Muñoz-Sabater, J., 2019. ERA5-Land Monthly Averaged Data from 1950 To Present.
Muñoz-Sabater, J., Dutra, E., Agustí-Panareda, A., Albergel, C., Arduini, G., Balsamo, G., Boussetta, S., Choulga, M., Harrigan, S., Hersbach, H., Martens, B., Miralles, D.G., Piles, M., Rodríguez-Fernández, N.J., Zsoter, E., Buontempo, C., Thépaut, J.N., 2021. ERA5-Land: a state-of-the-art global reanalysis dataset for land applications. Earth Syst. Sci. Data 13, 4349–4383.
National Climate Centre, 2024a. Major Weather and Climate Disaster Events In China.
National Climate Centre, 2024b. Major Weather and Climate Disaster Events in July in China.
Pan, Y., Zhang, C., Gong, H., Yeh, P.J.F., Shen, Y., Guo, Y., Huang, Z., Li, X., 2017. Detection of human-induced evapotranspiration using GRACE satellite observations in the Haihe River basin of China. Geophys. Res. Lett. 44, 190–199.
Pan, Y., Zhang, X., Jiao, J., Xiao, Y., 2024. Spatiotemporal variability at seasonal and interannual scales of terrestrial water variation over Tibetan Plateau from geodetic observations. Geo-spatial Inf. Sci. 1–16.
Park, J., van den Ijssel, J., Siemes, C., 2023. Dayside upper-thermospheric density fluctuations as observed by GRACE and GRACE-FO at ~500 km height. J. Geophys. Res. Space Phys. 128.
Peltier, W.R., Argus, D.F., Drummond, R., 2018. Comment on "An assessment of the ICE-6G_C (VM5a) glacial isostatic adjustment model" by Purcell et al. Journal of Geophysical Research: Solid Earth 123, 2019–2028.
Qiao, Y., Xu, W., Meng, C., Liao, X., Qin, L., 2022. Increasingly dry/wet abrupt alternation events in a warmer world: Observed evidence from China during 1980–2019. Int. J. Climatol. 42, 6429–6440.
Qin, D., Ding, Y., Su, J., Ren, J., Wang, S., Wu, R., Yang, X., Wang, S., Liu, S., Dong, G., Lu, Q., Huang, Z., Du, B., Luo, Y., 2005. Assessment of climate and environmental changes in China (I): climate and environment changes in China and their projection. Adv. Clim. Chang. Res. 01, 4–9.
Qiu, C., Liu, H., Wan, C., Zhao, L., Wen, J., 2022. Tempo-spatial variation and cause analysis of rainstorms and related flood disasters in Shandong from 1984 to 2019. J. Catastrophol. 37, 57–63.
Ramillien, G., Frappart, F., Güntner, A., Ngo-Duc, T., Cazenave, A., Laval, K., 2006. Time variations of the regional evapotranspiration rate from Gravity Recovery and climate Experiment (GRACE) satellite gravimetry. Water Resour. Res. 42.
Ran, J., Ditmar, P., van den Broeke, M.R., Liu, L., Klees, R., Khan, S.A., Moon, T., Li, J., Bevis, M., Zhong, M., Fettweis, X., Liu, J., Noel, B., Shum, C.K., Chen, J., Jiang, L., van Dam, T., 2024. Vertical bedrock shifts reveal summer water storage in Greenland ice sheet. Nature 635, 108–113.
Rodell, M., Famiglietti, J.S., Chen, J., Seneviratne, S.I., Viterbo, P., Holl, S., Wilson, C.R., 2004. Basin scale estimates of evapotranspiration using GRACE and other observations. Geophys. Res. Lett. 31.
Rodell, M., Famiglietti, J.S., Wiese, D.N., Reager, J.T., Beaudoing, H.K., Landerer, F.W., Lo, M.H., 2018. Emerging trends in global freshwater availability. Nature 557, 651–659.
Rodell, M., Li, B., 2023. Changing intensity of hydroclimatic extreme events revealed by GRACE and GRACE-FO. Nat. Water 1, 241–248.
Save, H., 2020. CSR GRACE and GRACE-FO RL06 Mascon Solutions v02.
Scanlon, B.R., Zhang, Z., Save, H., Sun, A.Y., Muller Schmied, H., van Beek, L.P.H., Wiese, D.N., Wada, Y., Long, D., Reedy, R.C., Longuevergne, L., Doll, P., Bierkens, M. F.P., 2018. Global models underestimate large decadal declining and rising water storage trends relative to GRACE satellite data. PNAS 115, E1080–E1089.
Shu, Z., Jin, J., Zhang, J., Wang, G., Lian, Y., Liu, Y., Bao, Z., Guan, T., He, R., Liu, C., Jing, P., 2024. 1.5℃ and 2.0℃ of global warming intensifies the hydrological extremes in China. J. Hydrol. 635, 131229.
Smith, A.B., 2024. 2023 US Billion-dollar weather and climate disasters in historical context, 104th Annual AMS Meeting 2024, p. 428624.
Smith, A.B., 2025. 2024: An active year of U.S. billion-dollar weather and climate disasters.
Sun, S., Shi, C., Pan, Y., Bai, L., Xu, B., Zhang, T., Han, S., Jiang, L., 2020a. Applicability assessment of the 1998–2018 CLDAS multi-source precipitation fusion dataset over China. J. Meteorolog. Res. 34, 879–892.
Sun, Z., Long, D., Yang, W., Li, X., Pan, Y., 2020b. Reconstruction of GRACE data on changes in total water storage over the global land surface and 60 basins. Water Resour. Res. 56.
Swain, D.L., Prein, A.F., Abatzoglou, J.T., Albano, C.M., Brunner, M., Diffenbaugh, N.S., Singh, D., Skinner, C.B., Touma, D., 2025. Hydroclimate volatility on a warming Earth. Nat. Rev. Earth Environ. 6, 35–50.
Swenson, S., Chambers, D., Wahr, J., 2008. Estimating geocenter variations from a combination of GRACE and ocean model output. J. Geophys. Res. Solid Earth 113.
Swenson, S., Wahr, J., 2006. Post-processing removal of correlated errors in GRACE data. Geophys. Res. Lett. 33.
Syed, T.H., Famiglietti, J.S., Rodell, M., Chen, J., Wilson, C.R., 2008. Analysis of terrestrial water storage changes from GRACE and GLDAS. Water Resour. Res. 44.
Tapley, B.D., Bettadpur, S., Ries, J.C., Thompson, P.F., Watkins, M.M., 2004. GRACE measurements of mass variability in the earth system. Science 305, 503–505.
Tapley, B.D., Watkins, M.M., Flechtner, F., Reigber, C., Bettadpur, S., Rodell, M., Sasgen, I., Famiglietti, J.S., Landerer, F.W., Chambers, D.P., Reager, J.T., Gardner, A. S., Save, H., Ivins, E.R., Swenson, S.C., Boening, C., Dahle, C., Wiese, D.N., Dobslaw, H., Tamisiea, M.E., Velicogna, I., 2019. Contributions of GRACE to understanding climate change. Nat. Clim. Chang. 9, 358–369.
United Nations, 2015. Sendai Framework for Disaster Risk Reduction 2015-2030.
Wang, H., Wang, S., Shu, X., He, Y., Huang, J., 2024a. Increasing occurrence of sudden turns from drought to flood over China. J. Geophys. Res. Atmos. 129, e2023JD039974.
Wang, W., Huang, H., Geng, H., Ma, M., Zhu, H., 2024b. National drought disaster prevention in China in 2024. China Flood Drought Manag. 34, 9–12.
Wasko, C., Nathan, R., Stein, L., O'Shea, D., 2021. Evidence of shorter more extreme rainfalls and increased flood variability under climate change. J. Hydrol. 603.
World Meteorological Organization, 2024. State of the Climate 2024, Geneva.
Wouters, B., Bonin, J.A., Chambers, D.P., Riva, R.E., Sasgen, I., Wahr, J., 2014. GRACE, time-varying gravity, Earth system dynamics and climate change. Rep. Prog. Phys. 77, 116801.

Wu, S., 2023. A systematic review of climate policies in China: Evolution, effectiveness, and challenges. Environ. Impact Assess. Rev. 99, 107030.
Xiao, C., Zhong, Y., Feng, W., Gao, W., Wang, Z., Zhong, M., Ji, B., 2023. Monitoring the catastrophic flood with GRACE-FO and near-real-time precipitation data in northern Henan Province of China in July 2021. IEEE J. Sel. Top. Appl. Earth Obs. Remote Sens. 16, 89–101.
Xie, J., Xu, Y.-P., Wang, Y., Gu, H., Wang, F., Pan, S., 2019. Influences of climatic variability and human activities on terrestrial water storage variations across the Yellow River basin in the recent decade. J. Hydrol. 579, 124218.
Xie, J., Xu, Y.-P., Yu, H., Huang, Y., Guo, Y., 2022. Monitoring the extreme flood events in the Yangtze River basin based on GRACE and GRACE-FO satellite data. Hydrol. Earth Syst. Sci. 26, 5933–5954.
Xinhua News, 2024a. China issues forecast for massive flooding in Guangdong. Xinhua News.
Xinhua News, 2024b. Floods above warning level occurred in 33 rivers in China.
Yang, F., Lu, H., Yang, K., He, J., Wang, W., Wright, J.S., Li, C., Han, M., Li, Y., 2017. Evaluation of multiple forcing data sets for precipitation and shortwave radiation over major land areas of China. Hydrol. Earth Syst. Sci. 21, 5805–5821.
Yang, S., Zhong, Y., Wu, Y., Yang, K., An, Q., Bai, H., Liu, S., 2025. Quantifying long-term drought in China's exorheic basins using a novel daily GRACE reconstructed TWSA index. J. Hydrol. 655.
Yin, J., Guo, S., Yang, Y., Chen, J., Gu, L., Wang, J., He, S., Wu, B., Xiong, J., 2022. Projection of droughts and their socioeconomic exposures based on terrestrial water storage anomaly over China. Sci. China Earth Sci. 65, 1772–1787.
Zhang, L., Sun, W., 2022. Progress and prospect of GRACE Mascon product and its application. Rev. Geophys. Planet. Phys. 53, 35–52.
Zhang, R., 2015. Changes in East Asian summer monsoon and summer rainfall over eastern China during recent decades. Sci. Bull. 60, 1222–1224.
Zhang, S., Chen, X., Su, C., Cui, Z., Wang, J., 2004. Analysis on the severe drought of Shandong Province in 2002. Hydrology 24, 42–45.
Zhang, W., Furtado, K., Wu, P., Zhou, T., Chadwick, R., Marzin, C., Rostron, J., Sexton, D., 2021. Increasing precipitation variability on daily-to-multiyear time scales in a warmer world. Sci. Adv. 7, eabf8021.
Zhang, W., Zhou, T., Wu, P., 2024. Anthropogenic amplification of precipitation variability over the past century. Science 385, 427–432.
Zhang, W., Zhou, T., Ye, W., Zhang, T., Zhang, L., Wolski, P., Risbey, J., Wang, Z., Min, S.-K., Ramsay, H., Brody, M., Grimm, A., Clark, R., Ren, K., Jiang, J., Chen, X., Fu, S., Li, L., Tang, S., Hu, S., 2025. A year marked by extreme precipitation and floods: weather and climate extremes in 2024. Adv. Atmos. Sci.
Zhang, X., Luo, J., Chen, L., Li, H., 2000. Zoning of chinese flood hazard risk. J. Hydraul. Eng. 3, 1–7.
Zhang, Y., Liang, S., Ma, H., He, T., Wang, Q., Li, B., Xu, J., Zhang, G., Liu, X., Xiong, C., 2023. Generation of global 1 km daily soil moisture product from 2000 to 2020 using ensemble learning. Earth Syst. Sci. Data 15, 2055–2079.
Zheng, J., Bian, J.J., Ge, Q., Hao, Z., Yin, Y., Liao, Y., 2013. The climate regionalization in China for 1981–2010. Chin. Sci. Bull. 58, 3088–3099.
Zhong, Y., Bai, H., Feng, W., Lu, J., Humphrey, V., 2023. Separating the precipitation- and non-precipitation- driven water storage trends in China. Water Resour. Res. 59.
Zhong, Y., Tian, B., Kim, H., Yuan, X., Liu, X., Zhu, E., Wu, Y., Wang, L., Wang, L., 2025. Over 60% precipitation transformed into terrestrial water storage in global river basins from 2002 to 2021. Commun. Earth Environ. 6.
Zhou, B., 2024. Why is extreme weather becoming more and more frequent and how can we deal with it?, In: Li, X. (Ed.), Minsheng Weekly.
Zou, A., Yang, Y., Wang, H., Wang, P., Liao, H., 2025. Aerosol decline accelerates the increasing extreme precipitation in China. Geophys. Res. Lett. 52, e2024GL113887.